RSC Applied Interfaces

ROYAL SOCIETY OF CHEMISTRY

COMMUNICATION

View Article Online
View Journal | View Issue

Cite this: *RSC Appl. Interfaces*, 2026, 3, 333

Received 19th August 2025,
Accepted 8th January 2026

DOI: 10.1039/d5lf00247h

rsc.li/RSCApplInter

Surface-interactive control of apatite nanoparticles with albumin

Kazuto Sugimoto,[ab] Ryota Akutsu,[a] Zizhen Liu,[ac] Shimon Konosu[a] and Motohiro Tagaya *[a]

The adsorption behavior of albumin (Alb) on the apatite nanoparticles synthesized using different pH-adjusters was investigated in biological fluid. The nanoparticles synthesized using KOH induced the most elastic Alb adsorption through the non-apatitic surface nanolayer, indicating that the Alb adsorption states can be effectively tuned by selecting the appropriate pH-adjuster during nanoparticle synthesis.

Biocompatible materials can be incorporated into biomedical devices to allow safe implantation into the human body, thereby promoting enhanced cell adhesion and tissue formation.[1] When biocompatible materials are implanted, a three-layered structure is typically formed on their surfaces.[2,3] First, a hydration layer is formed, followed by protein adsorption and subsequent cell adhesion, which is considered to play an important role in the biocompatible material–tissue interactions. However, under the simplified *in vitro* conditions, when biocompatible materials are immersed in biological fluids, the cell-non-adhesive protein (albumin (Alb)) is abundantly adsorbed, which can potentially inhibit subsequent cell adhesion and spreading.[4,5] During the adsorption, a decrease in the α-helix fraction of Alb accompanied by unfolding has been reported, leading to a reduction in its higher-order conformational state.[6,7] Accordingly, the mechanistic studies under controlled conditions are required *in vitro* to clarify how the biocompatible material composition and crystallinity influence the Alb adsorption behavior on the surfaces.

Hydroxyapatite (HA, $Ca_{10}(PO_4)_6(OH)_2$) is an inorganic component of bone and is highly biocompatible. HA prepared by wet chemical methods often forms nanoparticles which are covered with the non-apatitic layer.[8,9] The non-apatitic layer contains an amorphous phase composed of phosphate, calcium, and carbonate ions, together with a hydration layer. Consequently, HA nanoparticles are reported to exhibit higher reactivity and excellent affinity toward osteoblasts and osteoclasts.[10,11] The hydration layer is formed through the interactions between hydrated ions and water molecules, which affects the protein adsorption and cell adhesion.[12,13] The hydration layer is typically classified into three categories according to the strength of interaction with biocompatible material surfaces: (i) non-freezing water, (ii) intermediate water, and (iii) free water, in descending order of interaction strength. Our group has found that the hydration layer changes depending on the presence of ions in HA, and these states are expected to affect the protein adsorption layer and cell adhesion.[14] Therefore, it is possible to regulate the adsorption structure of Alb by modulating the hydration layer through trace amounts of ions added during HA synthesis. However, no systematic studies have investigated the effects of the ions present in the non-apatitic layer of HA nanoparticles on the higher-ordered structure of Alb, and the adsorption mechanism therefore remains unclear. The present study is original in that it provides a new materials design guideline based on the functionalization of non-adhesive proteins through a controlled hydration layer state.

We successfully synthesized HA nanoparticles with trace ions introduced depending on the pH adjusting agents ((i) trimethylammonium hydroxide (TM), (ii) NaOH (Na), and (iii) KOH (K)) during the synthesis.[15] In this study, the nanoparticles with a higher PO_4^{3-} fraction in the non-apatitic layer were deposited as a film onto a gold (Au) surface to investigate Alb adsorption. Specifically, the nanoparticles were dispersed in phosphate buffer (PB), and their composition and surface charge states were evaluated. The adsorption behavior of Alb on the nanoparticle film was evaluated using a quartz crystal microbalance with dissipation (QCM-D), and the secondary structure of Alb was also

[a] *Department of Materials Science and Bioengineering, Graduate School of Engineering, Nagaoka University of Technology, 1603-1 Kamitomioka, Nagaoka 940-2188, Japan. E-mail: tagaya@mst.nagaokaut.ac.jp*
[b] *Japan Society for the Promotion of Science (JSPS) Research Fellowship for Young Scientists (DC), 5-3-1 Koji-machi, Chiyoda-ku, Tokyo 102-0083, Japan*
[c] *Japan Society for the Promotion of Science (JSPS) Research Fellowship for Young Scientists (PD), 5-3-1 Koji-machi, Chiyoda-ku, Tokyo 102-0083, Japan*

analyzed. The results obtained from the above studies clarified the relationship between the ions contained in the HA nanoparticles and the adsorption state of Alb (Scheme 1).

The HA nanoparticles were synthesized according to the previous report on TM-10, Na-10, and K-10.[15] Subsequently, a phosphate buffer (PB) immersion experiment was conducted to allow Alb adsorption on the nanoparticle surfaces. In particular, 400 mg of each nanoparticle was pre-dried, dispersed in 40 mL of PB, and stirred at 37 °C for 1.5 h. The solid phase was separated, washed with deionized water, and lyophilized. The resulting solid was named X-10-PB (X = TM, Na, K), depending on the type of pH-adjuster used.

For the Alb adsorption experiment, after immersion in PB for 1.5 h, each nanoparticle was immediately incubated with Alb at a concentration of 1 mg mL^{-1} in PB at 37 °C for 3 h. The final solid was separated, washed with deionized water, lyophilized, and designated as X-10-Alb (X = TM, Na, K). As the control, the nanoparticles that were continuously immersed in PB for 4.5 h, then washed with deionized water, and lyophilized, were designated as X-10-PB/ref (X = TM, Na, K).

The nanoparticles obtained from the PB immersion experiment were evaluated using X-ray fluorescence (XRF), zeta potential measurements, and X-ray diffraction (XRD). The detailed procedures are described in Experimental Procedure S1.

The Fourier transform infrared (FT-IR) spectral separation of the hydration layer was performed based on the peak positions shown in Tables S1 and S2, and subsequently analyzed, as described in Experimental Procedure S2.

The Alb adsorption was evaluated by quartz crystal microbalance with dissipation (QCM-D). The HA thin film was prepared according to a previously reported method.[15] The evaluation procedure was performed by flowing PB and Alb solutions over the HA thin film in the same manner as described for the Alb adsorption experiments above. The Alb adsorption process and the higher-order structure of the adsorbed protein were evaluated by monitoring the Δf and ΔD curves using the QCM-D technique (Fig. S1–S3), as described in Experimental Procedure S3.

The secondary structure of the Alb adlayer was analyzed by FT-IR spectroscopy. In the evaluation of the Alb adsorption layer, difference spectra were obtained by subtracting the spectra of X-10-PB from those of X-10-Alb and analyzed (Fig. S4). For the spectral separation, eight peaks derived from the protein secondary structures were evaluated (Fig. S5 and Table S3), as described in the Experimental Procedure S4.

The cation content of the HA nanoparticles before and after PB immersion was examined using XRF (Fig. 1(a)). In all cases, the reduction in the overall cation content was observed following immersion, indicating cation release into

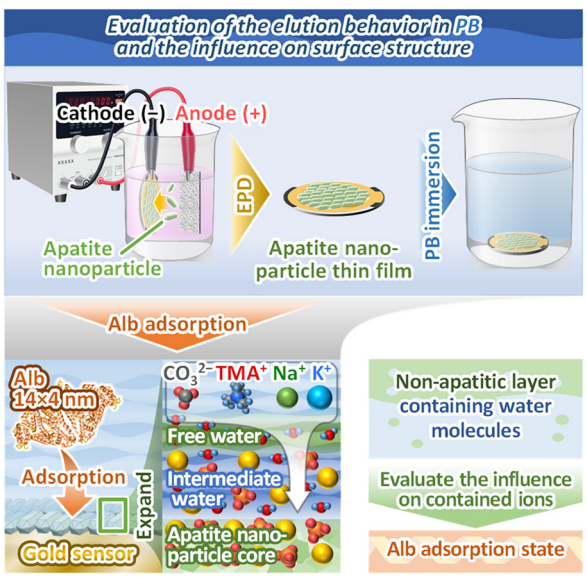

Scheme 1 Illustration of the reaction behavior of the apatite nanoparticle film in PB and the Alb adsorption on the surface in this study.

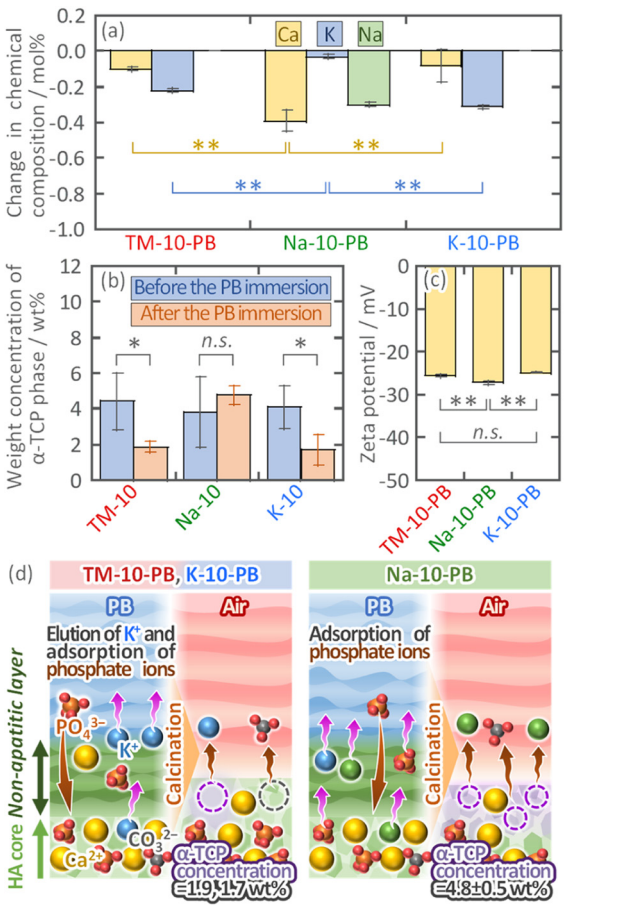

Fig. 1 (a) Concentration changes in the chemical composition of the nanoparticles before and after PB immersion, as measured by XRF. (b) Weight concentration of the α-TCP phase before and after PB immersion calculated from the XRD patterns (Fig. S6) using RIR quantification. (c) Zeta potential values of the nanoparticles in PB. (d) Illustrations of the elution behavior of the nanoparticles during PB immersion and the subsequent phase changes upon calcination. Here, Student's *t*-test results were presented by $p < 0.05$ (*), $p < 0.01$ (**), and non-significant (n.s.).

PB. Due to the different trends in the extent of reduction, the discussion was divided into two groups: TM-10 and K-10 *versus* Na-10.

In TM-10 and K-10, the concentrations of Ca and K decreased after PB immersion, whereas Na was not detected. The markedly greater reduction in K compared to Ca suggests that K^+ was enriched on the nanoparticle surfaces and preferentially released upon immersion. In contrast, Na-10 exhibited the substantial decrease in both Ca and Na, with only a slight decrease in K. Since the ionic radius of Na^+ is similar to that of Ca^{2+}, it is more stably incorporated into both the crystalline lattice and the nanoparticle surfaces during synthesis. Conversely, K^+, which has a larger ionic radius than Ca^{2+}, is less readily incorporated.[16,17] Thus, the pronounced cation release observed for Na-10 is attributed to the abundant incorporation of Na^+ into both the bulk and the surface during synthesis.

These results indicated that the dissolution behavior is strongly dependent on the nature of the incorporated cations. In particular, the release of Ca^{2+} may result in the formation of Ca site vacancies on the surface, potentially inducing phase transitions. To investigate such structural alterations, all nanoparticles were calcined at 1200 °C, and the crystalline phases prior to calcination were inferred from XRD analyses (Fig. S6). The diffraction patterns revealed HA (ICDD No. 00-009-0432) as the primary phase and α-TCP (ICDD No. 00-009-0348) as the secondary phase. The weight fraction of the α-TCP phase was quantified using the RIR method (Fig. 1(b)). A decrease in the α-TCP content was observed for both TM-10 and K-10 after PB immersion. Previous studies have reported that the calcination of calcium-deficient hydroxyapatite (CDHA) or alkali-ion-substituted apatites (containing Na^+ or K^+) often results in the α-TCP phase formation.[18–21] Therefore, the suppression of α-TCP phase formation in TM-10 and K-10 is attributed to the elution of Na^+ and K^+ during PB immersion. Interestingly, Na-10 showed no significant change in the α-TCP phase content despite the marked cation release. This apparent contradiction is likely due to two counteracting effects: (1) suppression of α-TCP phase formation due to Na^+ elution, and (2) promotion of α-TCP formation *via* the HA-to-CDHA transition resulting from Ca^{2+} depletion on the nanoparticle surface. These effects may have offset one another, leading to no net change in the α-TCP content.

To assess the surface modifications caused by PB immersion, zeta potential was measured using phosphate-free aqueous solvents (saline: approximately −16 mV,[22–24] Bis-Tris buffer: approximately −7.5 mV (ref. 25)). The results suggest changes in the surface of all nanoparticles due to PB immersion (Fig. 1(c)). All nanoparticles exhibited pronounced negative zeta potentials, consistent with the presence of phosphate groups on the surface, which are known to act as potential-determining ions in HA.[26,27] No statistically significant difference was observed between TM-10-PB and K-10-PB, both showing values around −25 mV. This suggests that, although surface K^+ was leached, the dominant surface charge remained governed by the phosphate species. In contrast, Na-10-PB exhibited a more negative zeta potential than the other two nanoparticles, implying the enhanced elution of Ca^{2+}—another potential-determining ion in HA—alongside Na^+ and K^+. This Ca^{2+} depletion is thought to induce a surface phase transition towards a CDHA-like layer, contributing to the increased negative charge.[26,27]

In summary, PB immersion induced distinct dissolution and phase transition behaviors depending on the incorporated cation species. In TM-10 and K-10, K^+ located in the non-apatitic layer was selectively leached, suppressing the formation of the CDHA phase. However, in Na-10, the substantial release of Na^+, K^+, and Ca^{2+} simultaneously suppressed and promoted α-TCP formation, resulting in the surface transformation into a CDHA layer with an overall more negative surface charge (Fig. 1(d)).

When bioceramics are implanted in the body, the material surfaces interact with water molecules to form a hydration layer. Therefore, the hydration layer formed on the nanoparticle surfaces after PB immersion was evaluated by spectral separation of the O–H characteristic absorption band (2800–3800 cm^{-1}) in the FT-IR spectra. The results of the spectral separation and the area fractions of each component are shown in Fig. S7, and the plot of the free water component is shown in Fig. 2(a). TM-10-PB exhibited the highest percentage of free water, which was considered to be derived from the adsorption of TMA^+ ions on its surface. For more detailed component separation, the results of the vibrational components of water molecules in the hydration layer and the area fraction of each component are shown in Fig. S8. The trend of the highest component ratio of the asymmetric stretching vibration of O–H bonds in free water and the lowest component ratio of the symmetric stretching vibration of O–H bonds in intermediate water in TM-10-PB was similar to that in Fig. S7. The ratio of the vibrational components of O–H bonds of the water molecules (R_{as}) calculated from eqn (S1) is shown in Fig. 2(b). The asymmetrization of the stretching vibration of water molecules in the free water on TM-10-PB was predominant, which was attributed to the presence of TMA^+ ions on the TM-10-PB surface. The TMA^+ ions are negatively charged by the nitrogen atom at the center and positively charged by the

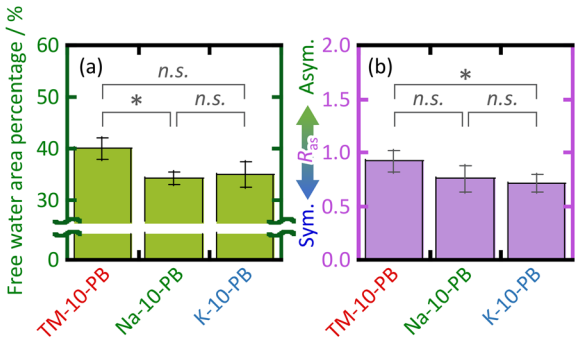

Fig. 2 Plots of (a) percentage of free water and (b) R_{as} of water molecules obtained from eqn (S1). Here, Student's *t*-test results were presented by $p < 0.05$ (*), $p < 0.01$ (**), and non-significant (n.s.).

four surrounding methyl groups (Scheme S1(a)). The electrostatic interactions of one or three methyl groups of TMA^+ ions with phosphate ions on the nanoparticle surface were considered to occur (Scheme S1(b)).[28] The TMA^+ ions adsorbed on the nanoparticle surface orient the remaining hydrophobic methyl groups towards the aqueous phase, resulting in the hydrophobic hydration structure surrounding them. The water molecules were close to the free water states, and the O–H bonding between water molecules became predominant, resulting in the asymmetrization of stretching vibration and contraction, which is believed to induce the formation of water clusters at the surface of the TMA^+ ions.[29]

It was found that the surface states of the apatite nanoparticles differed significantly depending on the type of pH adjuster used during the synthesis. Since the surface state differences possibly affected the Alb adsorption state, we evaluated the higher-order structures of the Alb adsorption process and the secondary structure states on the nanoparticles after adsorption. First, the adsorption of Alb on the film was measured using QCM-D. The ΔD–Δf curves and Δf and ΔD values at the end of the measurement are shown in Fig. S9. The final Δf and ΔD values did not differ significantly among the nanoparticles. For further evaluation, the $\Delta D/\Delta f$ plots were prepared, showing the $\Delta D/\Delta f$ values for "(1) the initial stage (*i.e.*, 10–100 min from the start of adsorption)" and "(2) the equilibrium stage (*i.e.*, 120–180 min from the start of adsorption)" (Fig. 3(a)). The $\Delta D/\Delta f$ value in the stage (1) showed a higher absolute slope for TM-10-PB as compared to the cases in the other nanoparticle films. Therefore, Alb was sterically adsorbed on TM-10-PB during the initial adsorption stage. The $\Delta D/\Delta f$ value changes between the initial (1) and the equilibrium (2) adsorption stages of the nanoparticle films were calculated from the angles of (2) relative to (1) (*i.e.*, rotation angle) using eqn (S2) based on the Experimental Procedure S3. Specifically, the rotation angle decreased in the order: TM-10-PB > Na-10-PB > K-10-PB. This trend suggests that the Alb adsorption layer underwent rearrangement (*i.e.*, conformational change) during the equilibrium stage, and the degree was decreased in the order: TM-10-PB > Na-10-PB > K-10-PB.

To evaluate the viscoelasticity at each stage, the Alb adsorption layer was analysed using the Voigt viscoelastic model based on the Δf and ΔD curves of each film. As shown in Fig. 3(b and e), the thickness of the Alb adsorption layer was approximately 12 nm, with no significant difference in either thickness or mass among the nanoparticles. Based on the thickness, the adsorption morphology of Alb was inferred to be predominantly end-on (*i.e.*, adsorbed in a standing orientation) rather than side-on (*i.e.*, in a flat-lying orientation),[30] which is consistent with the oval-shaped dimensions of Alb (14 × 4 × 4 nm). This end-on adsorption morphology is likely associated with the specific interactions between the functional groups on the top surface of Alb and the non-apatitic layer on the nanoparticle surface. In particular, the top surface of Alb was rich in hydrophilic amino acid residues. At pH 7.4 in PB, the imidazole and

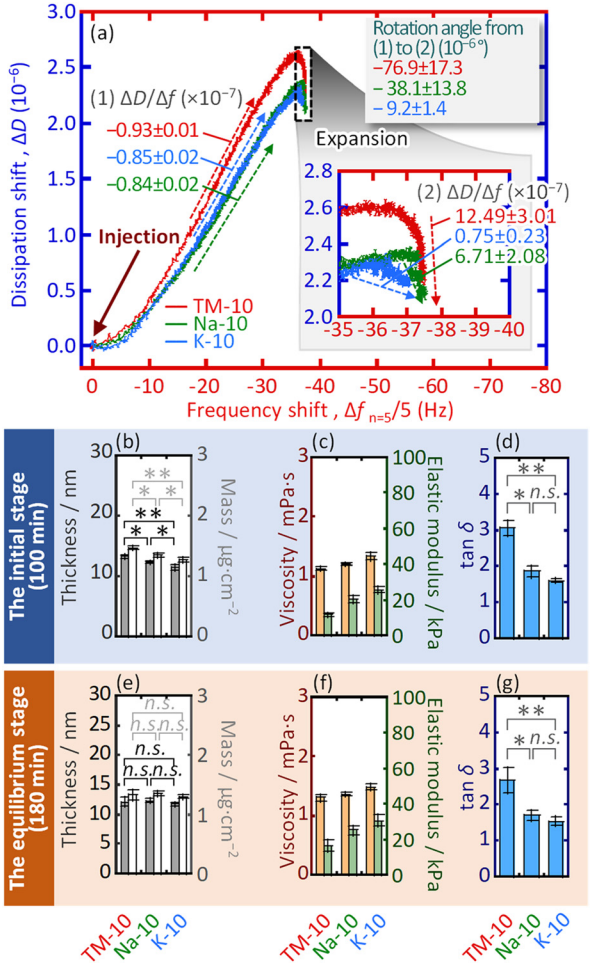

Fig. 3 (a) $\Delta D/\Delta f$ plots of the Alb adsorption process on the nanoparticle films for 3 h and magnified view of the adsorption equilibrium stages. Here, the $\Delta D/\Delta f$ values changed significantly between (1) 10–100 min and (2) 120–180 min. (b–g) Viscoelastic properties and film thicknesses of the hydration and Alb adsorption layers ((b and e) thickness and mass, (c and f) viscosity and elastic modulus and (d and g) tan δ). The values in (b–d) indicated the adsorption stage (at around 100 min), and those in (e–g) indicated the equilibrium stage (at around 180 min). Here, Student's *t*-test results were presented by $p < 0.05$ (*), $p < 0.01$ (**), and non-significant (n.s.).

carboxyl groups on the side chains of these residues were deprotonated and became negatively charged.[31,32] During immersion in PB, anions such as PO_4^{3-}, HPO_4^{2-}, and CO_3^{2-} within the non-apatitic layer were released *via* ion exchange with buffer ions. This process was thought to promote the adsorption of negatively charged Alb functional groups onto the nanoparticle surface from the viewpoint of charge compensation. Furthermore, the non-apatitic layer is hydrophilic and contains water molecules, suggesting that O–H bonding can occur between the layer and the hydrophilic amino acid residues on Alb. These O–H bonding states contribute to the hydrophilic interactions that stabilize the adsorbed layer. Overall, the results indicate that a stable Alb adsorption layer would be formed through a combination of electrostatic interactions between the negatively charged

Alb groups and calcium (Ca^{2+}) sites of the HA structure, as well as he O–H bonding between the hydrophilic groups of Alb and the water-containing non-apatitic layer.[33,34] These interactions favour the end-on adsorption configuration in which Alb stands upright on the film, leading to an estimated layer thickness of approximately 12 nm.[35,36] In particular, for the Na-10-PB condition, additional interfacial interactions may be involved. Trace amounts of amino and guanidino groups, found in the residues such as lysine and histidine on the Alb surface, can become positively charged and interact with Ca-deficient sites on the nanoparticles, thereby further promoting adsorption.[31,32]

The following section discusses the Alb adsorption states on the films. The viscosity and elastic modulus during the initial stage (Fig. 3(c)) were the highest for K-10-PB, followed by Na-10-PB, and then TM-10-PB. At the equilibrium stage (Fig. 3(f)), both viscosity and elastic modulus increased for all the films as compared to the initial stage. This increase at equilibrium is attributed to conformational changes in the protein upon adsorption, which enhance the rigidity (*i.e.*, higher modulus) and increase the number of interaction points with surrounding water molecules.[37,38] To further investigate the viscoelastic behaviors, the $\tan\delta$ values (the ratio of viscosity to elasticity) were calculated for both the initial and equilibrium stages (Fig. 3(d and g)) using eqn (S3) based on the Experimental Procedure S3. The results showed that $\tan\delta$ decreased in the order of TM-10-PB > Na-10-PB > K-10-PB, and all nanoparticles exhibited lower $\tan\delta$ values at the equilibrium stage compared to the case in the initial stage. This variation in $\tan\delta$ among the nanoparticles was attributed to the differences in the surface properties of the apatite-based films. For TM-10-PB, water molecule clusters associated with adsorbed TMA^+ ions on the nanoparticle surface weakened the interaction between Alb and the surface, leading to the formation of a viscous (less elastic) adsorption layer.[29] For Na-10-PB, the strong negative surface charge of the CDHA film increased the electrostatic repulsion with negatively charged Alb, resulting in a more viscous adsorption layer. In contrast, K-10-PB retained a surface structure more similar to that of stoichiometric HA, resulting in the adsorption behavior more comparable to typical HA–protein interactions.[39,40]

To evaluate the secondary structure of the adsorbed Alb, the peak separation in the amide I region (1600–1700 cm^{-1}) of the FT-IR spectra was performed as shown in Fig. S10(a). The calculated area fraction of each component and the denaturation state of Alb were determined using eqn (S4) based on the Experimental Procedure S4, and are presented in Fig. S10(b). The area percentages of the α-helix structure for the adsorbed Alb on the film were 22.5 ± 0.2% for TM-10-Alb, 22.6 ± 0.5% for Na-10-Alb, and 21.9 ± 0.4% for K-10-Alb, respectively. Based on the previous report, the α-helix content of native Alb in PB is approximately 54.7%, suggesting that the adsorption on the film led to significant unfolding.[41,42] The calculated denaturation state was approximately 1.2 for all films, which is considerably higher than the reported value of 0.32 for the Alb in PB, indicating the structural disruption during adsorption. Therefore, when Alb was adsorbed on the apatite nanoparticles, it underwent conformational changes involving unfolding and denaturation. Since Alb has been reported to convert into a cell-adhesive state when its α-helix content falls below 47%,[3–7] we conclude that the adsorbed Alb on the film in this study is likely in such a state.

To elucidate the mechanism of Alb adsorption on the nanoparticle films, the schematic illustrations of the interfacial reactions and surface states upon the immersion in PB are presented in Scheme S2. In TM-10, the presence of TMA^+ ions in the non-apatitic layer promoted the formation of water molecule clusters, which increased the free water fraction within the hydration layer. This enhanced hydration weakened the intermolecular interactions between the film and Alb, resulting in the steric-dominated adsorption. At the equilibrium stage, the weakened interaction likely facilitates the molecular rearrangement of Alb. For Na-10, immersion in PB induces leaching of surface-bound cations (*i.e.* Ca^{2+}, Na^+, and K^+), leading to exposure of the CDHA core, which is strongly negatively charged. As a result, electrostatic repulsion between the negatively charged Alb molecules and the CDHA surface becomes dominant, leading to a weak viscous-type adsorption state. Although the adsorption strength is lower, a slight rearrangement of Alb is inferred to occur at the equilibrium stage due to the continued repulsive forces. In contrast, K-10 retained its HA surface structure despite K^+ leaching from the non-apatitic and near-surface layers. This stable HA surface enabled the strong interactions with Alb, likely mediated by a combination of ionic and O–H bonding. At the equilibrium stage, the strong binding affinity was presumed to limit the extent of Alb rearrangement, suggesting a relatively elastic adsorption state. It can be concluded that all the nanoparticles exhibited Alb adsorption, accompanied by a certain degree of structural unfolding. In particular, K-10 enabled the most elastic adsorption form, likely denaturing the higher-order structure of Alb. This feature possibly accounts for the superior cell adhesion of K-10, as structurally denatured Alb tends to retain higher bioactivity at the interface.

Conclusions

In summary, we systematically compared the surface reactivity and Alb adsorption of apatite nanoparticle films synthesized using three pH adjusters (TMAOH, NaOH, and KOH) in biological fluids. The TMAOH-derived film, enriched with water-coordinated TMA^+ clusters, increased the free water fraction in the hydration layer, resulting in weakened Alb binding. The surface of the NaOH-derived film was transformed into a CDHA layer in phosphate buffer, leading to a moderately viscous Alb layer. The KOH-derived films retained their HA surface after immersion and bound Alb as tightly as on stoichiometric HA surfaces, exhibiting the most elastic adsorption for K-10. The Alb rearrangement (*i.e.*,

mobility) on the surfaces followed the order of TMAOH > NaOH > KOH. These findings were significant in that they demonstrated, for the first time, that the ionic species in the non-apatitic layer of the HA nanoparticles could simultaneously regulate the hydration structures and the Alb adsorption behavior. The ion-controlled apatite design strategy proposed in this study enables the precise control over the structural integrity of cell-non-adhesive proteins and is therefore applicable to the development of novel implant coating technologies, drug delivery system carriers, and scaffold materials.

Author contributions

Conceptualization, K. S. and M. T.; methodology, K. S., R. A., Z. L., S. K. and M. T.; software, K. S., S. K. and R. A.; validation, R. A. and M. T.; formal analysis, K. S., R. A. and M. T.; investigation, K. S., S. K. and M. T.; resources, M. T.; data curation, K. S. and M. T.; writing – original draft preparation, K. S. and M. T.; writing – review and editing, Z. L., S. K. and M. T.; supervision, M. T.; project administration, M. T. All authors have read and agreed to the published version of the manuscript.

Conflicts of interest

There are no conflicts to declare.

Data availability

The data that support the findings of this paper are available from the corresponding author upon reasonable request.

Supplementary Information (SI): detailed experimental procedures (Experimental Procedure S1–S4). Peak assignment of three different hydration layers on the apatite nanoparticles in the FT-IR spectra (Table S1). Peak assignment of five different vibrational states of the hydration layers on the apatite nanoparticles in the FT-IR spectra, which were obtained by collecting the vibration components possibly interacting with the HA surfaces after precise peak separation (Table S2). Illustration of measurement of Alb adsorption behavior on the apatite nanoparticles using QCM-D sensor, and typical rapid excitation of the QCM-D near resonance, followed by an exponentially damped sinusoidal wave after rapid disconnection, which can be fitted to calculate τ (Fig. S1). Representative images of ΔD and Δf curves, and the ΔD–Δf plots. Schematic illustration of the geometry and parameters used to simulate the hydrated layers and Alb adlayer on apatite nanoparticles film located between the QCM-D sensor surface and a semi-infinite Newton liquid (Fig. S2). Calculation method for the slope angles in (1) the initial stage and (2) the equilibrium stage in the ΔD–Δf plot. From the $m_{ini.}$ and $m_{eq.}$ in the initial and equilibrium stages, the $\theta_{ini.}$ and $\theta_{eq.}$ in the initial and equilibrium stages were calculated as shown in inset (Fig. S3). Representative differential spectrum illustrating removal of O–H stretching vibration and isolation of the amide I band, obtained by subtracting the X-10-PB/ref spectrum from the X-10-Alb spectrum (Fig. S4). Second derivatives of the FT-IR spectra in the amide I region of the Alb adlayer on the apatite nanoparticles (Fig. S5). Peak assignment of the amide I band in the FT-IR spectra of Alb layer on the apatite nanoparticles (Table. S3). XRD patterns of the apatite nanoparticles after the immersion in PB and calcination at 1200 °C (Fig. S6). Curve fitting and spectral separation results of four components of the O–H absorption bands in the FT-IR spectra of the nanoparticles. The detailed assignments for X-10-PB are provided in Table S1. Area percentage of three types of hydration layers formed on the nanoparticles after immersion in PB (Fig. S7). Curve fitting and spectral separation results of five components of the O–H absorption bands in the FT-IR spectra of the nanoparticles. The detailed assignments are provided in Table S2. Area percentage of four types of hydration layers formed on the nanoparticles after immersion in PB (Fig. S8). Illustration of the pseudospherical charge distribution of the TMA ion, and the coordination states of TMA ions with phosphate ions in the HA core, estimated from the charges and H_2O states (Scheme S1). ΔD and Δf curves with the Alb adsorption on the nanoparticle films (Fig. S9). Curve fitting and spectral separation results of seven components of the amide I bands of the nanoparticles in the FT-IR spectra. The detailed assignments are provided in Table S3. Area percentages of secondary structure components in the Alb adsorption layer obtained from, and the degree of Alb denaturation calculated from eqn (S3). Reference values of secondary structure percentages in solution: α-helix = 54.7%, β-sheet = 6.7%, Random = 19.8%, β-turn = 7.6% (Fig. S10). Illustration of the changes in the surface states of the nanoparticles during PB immersion and during the initial and equilibrium stages of the Alb adsorption, as supported by the measured values in this study (Scheme S2). See DOI: https://doi.org/10.1039/d5lf00247h.

Acknowledgements

This study was partially supported by a grant from the Japan Society for the Promotion of Science (JSPS) KAKENHI (Grant-in-Aid for Scientific Research(B), grant no. 25K01741, Grant-in-Aid for JSPS Fellows, grant no. 25KJ1344, and Grant-in-Aid for JSPS Fellows, grant no. 24KJ1174), and Iketani Science and Technology Foundation (Grant Number 0371177-A). The authors thank the Analysis and Instrumentation Center in Nagaoka University of Technology for providing the facilities.

References

1 Q. Zhao, C. Li, H. C. Shum and X. Du, *Lab Chip*, 2020, **20**, 4321–4341.
2 Y. Ito, M. Sisido and Y. Imanishi, *J. Biomed. Mater. Res.*, 1990, **24**, 227–242.

3 M. Tanaka, T. Motomura, M. Kawada, T. Anzai, Y. Kasori, T. Shiroya, K. Shimura, M. Onishi and A. Mochizuki, *Biomaterials*, 2000, **21**, 1471–1481.
4 J. Nakanishi, Y. Kikuchi, T. Takarada, H. Nakayama, K. Yamaguchi and M. Maeda, *J. Am. Chem. Soc.*, 2004, **126**, 16314–16315.
5 Y. Xiao and S. N. Isaacs, *J. Immunol. Methods*, 2012, **384**, 148–151.
6 B. Sivaraman and R. A. Latour, *Langmuir*, 2012, **28**, 2745–2752.
7 H. Yamazoe, *J. Biosci. Bioeng.*, 2019, **127**, 515–519.
8 C. Rey, C. Combes, C. Drouet, H. Sfihi and A. Barroug, *Mater. Sci. Eng., C*, 2007, **27**, 198–205.
9 J. M. Delgado-López, M. Iafisco, I. Rodríguez, A. Tampieri, M. Prat and J. Gómez-Morales, *Acta Biomater.*, 2012, **8**, 3491–3499.
10 Y. Cai, Y. Liu, W. Yan, Q. Hu, J. Tao, M. Zhang, Z. Shi and R. Tang, *J. Mater. Chem.*, 2007, **17**, 3780–3787.
11 K. Fox, P. A. Tran and N. Tran, *ChemPhysChem*, 2012, **13**, 2495–2506.
12 M. Tanaka, T. Hayashi and S. Morita, *Polym. J.*, 2013, **45**, 701–710.
13 A. Mollahosseini and A. Abdelrasoul, *Biomed. Eng. Adv.*, 2022, **3**, 100034.
14 K. Sugimoto, K. Mikami, R. Kimura and M. Tagaya, *Langmuir*, 2023, **39**, 9431–9438.
15 K. Sugimoto, R. Akutsu, S. Yamada, T. G. Peñaflor Galindo and M. Tagaya, *ACS Appl. Mater. Interfaces*, 2025, **17**, 7131–7141.
16 R. D. Shannon, *Acta Crystallogr., Sect. A: Found. Crystallogr.*, 1976, **32**, 751–767.
17 K. Matsunaga and H. Murata, *Mater. Trans.*, 2009, **50**, 1041–1045.
18 R. G. Carrodeguas and S. De Aza, *Acta Biomater.*, 2011, **7**, 3536–3546.
19 J. Kolmas, A. Kaflak, A. Zima and A. Ślósarczyk, *Ceram. Int.*, 2015, **41**, 5727–5733.
20 S. Kannan, J. M. G. Ventura and J. M. F. Ferreira, *Ceram. Int.*, 2007, **33**, 1489–1494.
21 S. Kannan, J. M. G. Ventura, A. F. Lemos, A. Barba and J. M. F. Ferreira, *Ceram. Int.*, 2008, **34**, 7–13.
22 A. Doostmohammadi, A. Monshi, R. Salehi, M. H. Fathi, Z. Golniya and A. U. Daniels, *Ceram. Int.*, 2011, **37**, 2311–2316.
23 A. Naqshbandi and A. Rahman, *Mater. Lett.*, 2022, **312**, 131698.
24 A. Naqshbandi and A. Rahman, *Ceram. Int.*, 2022, **48**, 8112–8117.
25 V. Uskoković, R. Odsinada, S. Djordjevic and S. Habelitz, *Arch. Oral Biol.*, 2011, **56**, 521–532.
26 G. Yin, Z. Liu, J. Zhan, F. Ding and N. Yuan, *Chem. Eng. J.*, 2002, **87**, 181–186.
27 X. Zhu, H. Fan, D. Li, Y. Xiao and X. Zhang, *J. Biomed. Mater. Res., Part B*, 2007, **82**, 65–73.
28 D. M. Gil, J. Echeverría and S. Alvarez, *Inorg. Chem.*, 2022, **61**, 9082–9095.
29 K. Ishihara, M. Mu, T. Konno, Y. Inoue and K. Fukazawa, *J. Biomater. Sci., Polym. Ed.*, 2017, **28**, 884–899.
30 M. Tencer, R. Charbonneau, N. Lahoud and P. Berini, *Appl. Surf. Sci.*, 2007, **253**, 9209–9214.
31 S. Servagent-Noinville, M. Revault, H. Quiquampoix and M.-H. Baron, *J. Colloid Interface Sci.*, 2000, **221**, 273–283.
32 M. Kawano and J. Hwang, *Clays Clay Miner.*, 2010, **58**, 272–279.
33 P. Hampitak, D. Melendrez, M. Iliut, M. Fresquet, N. Parsons, B. Spencer, T. A. Jowitt and A. Vijayaraghavan, *Carbon*, 2020, **165**, 317–327.
34 T. Kawasaki, *J. Chromatogr. A*, 1991, **544**, 147–184.
35 H. T. M. Phan, S. Bartelt-Hunt, K. B. Rodenhausen, M. Schubert and J. C. Bartz, *PLoS One*, 2015, **10**, e0141282.
36 T. Wangkam, S. Yodmongkol, J. Disrattakit, B. Sutapun, R. Amarit, A. Somboonkaew and T. Srikhirin, *Curr. Appl. Phys.*, 2012, **12**, 44–52.
37 J. Clarke and L. S. Itzhaki, *Curr. Opin. Struct. Biol.*, 1998, **8**, 112–118.
38 A. Caflisch and M. Karplus, *J. Mol. Biol.*, 1995, **252**, 672–708.
39 G. Dong, L. He, D. Pang, L. Wei and C. Deng, *Ceram. Int.*, 2016, **42**, 18648–18656.
40 M. Tagaya, T. Ikoma, T. Takemura, N. Hanagata, T. Yoshioka and J. Tanaka, *Langmuir*, 2011, **27**, 7645–7653.
41 K. V. Abrosimova, O. V. Shulenina and S. V. Paston, *J. Phys.: Conf. Ser.*, 2016, **769**, 012016.
42 H. Shen, Z. Gu, K. Jian and J. Qi, *J. Pharm. Biomed. Anal.*, 2013, **75**, 86–93.